npj | biomedical innovations

Article

https://doi.org/10.1038/s44385-025-00062-6

Integrated respiratory functions predict myelin status in the mouse brain

Check for updates

Kou Nishikubo[1], Kaho Hitomi[2], Reiichi Sugihara[2], Kyoka Higuchi[1], Lili Quan[1], Akiko Uyeda[1], Masaaki Nameta[3], Kentaro Okuyama[3], Shinsuke Shibata[3], Yuki Kato[2,4] ✉ & Rieko Muramatsu[1] ✉

Demyelination is a common pathological feature of central nervous system (CNS) diseases, and its early detection is important for the diagnosis of neurological disorders; therefore, simple detection methods are in high demand. In this study, we found that both age-related myelin loss and demyelination in disease model mice can be predicted through integrative analysis of multiple respiratory parameters. Changes in some respiratory parameters correlated with myelin levels with aging; however, integrative analysis using conventional models further enabled the prediction of age-related myelin changes. In cuprizone-induced demyelination models, average respiratory values did not differ between demyelinated and control mice. However, the integrative analysis of the respiratory parameter set successfully distinguished demyelinated mice. Our study showed that respiratory function data may be used as a non-invasive method to predict brain conditions in mice, although translation to humans will require further validation. This approach shows promise as a potential method for early disease prediction and diagnostic support for CNS diseases.

Myelin is a structure formed by oligodendrocytes, a type of glial cell in the central nervous system (CNS), and is an essential component of neural circuits. It ensheathes neuronal axons, enabling saltatory propagation that accelerates neural transmission and contributes to the maintenance of neural network homeostasis by providing metabolic and trophic support to axons. Therefore, alterations in myelin quantity or structure are considered to have a direct impact on neural function[1]. Demyelination, characterized by the loss or degradation of myelin, is a hallmark pathological change in CNS diseases such as multiple sclerosis (MS)[2] and Alzheimer's disease (AD)[3,4]. In addition, myelin abnormalities have been reported to be associated with aging[5], excessive physical activity[6], and even peripheral, non-neurological diseases[7–9], leading to white matter damage in the brain. Clinically, early remyelination is crucial for preserving neural function, as prompt myelin repair is expected to mitigate axonal degeneration and prevent irreversible neurological deficits[10]. Thus, accurate assessment of myelin status is considered beneficial for early diagnosis and timely therapeutic intervention. However, current methods for detecting myelin status in humans rely on positron emission tomography (PET) and diffusion magnetic resonance imaging (MRI)[11], both of which have significant limitations in terms of accessibility, simplicity, and cost-effectiveness. MRI requires prolonged stillness, while PET involves the administration of radioactive tracers, both of which impose considerable physical and time burdens on patients. Furthermore, image analysis demands specialized expertise, making these methods unsuitable for simple or routine screening. Given these limitations, there is a growing need, both in clinical and research contexts, for simple, cost-effective methodologies capable of reliably predicting myelin status.

Myelin content fluctuations are closely linked to the developmental dynamics of oligodendrocytes. Oligodendrocytes are formed through the differentiation of their precursor cells, oligodendrocyte precursor cells (OPCs), which are widely distributed throughout the CNS. Myelination begins with the proliferation of OPCs, followed by differentiation into mature oligodendrocytes, and subsequent ensheathment of axons, which requires extensive lipid synthesis[12]. Traditionally, research on myelination mechanisms has been primarily focused on molecular and cellular roles within the CNS. For instance, leukemia inhibitory factor (LIF) derived from astrocytes promotes OPC differentiation[13], while brain-derived neurotrophic factor (BDNF) released from activated neurons stimulates OPCs to myelinate[14]. The emphasis on CNS-derived molecular regulation of myelination stems from the long-standing view that the brain, protected by the blood-brain barrier (BBB), is functionally isolated from peripheral organs. However, recent advances in inter-organ communication research have revealed that CNS function can be modulated by systemic physiological states and peripheral signals. For instance, the gut microbiota, such as *Bacteroidetes* and *Firmicutes*, are linked to cognitive impairment, depending

[1]Department of Molecular Pharmacology, National Institute of Neuroscience, National Center of Neurology and Psychiatry, Tokyo, Japan. [2]Department of RNA Biology and Neuroscience, Graduate School of Medicine, The University of Osaka, Osaka, Japan. [3]Division of Microscopic Anatomy, Graduate School of Medical and Dental Sciences, Niigata University, Niigata, Japan. [4]Integrated Frontier Research for Medical Science Division, Institute for Open and Transdisciplinary Research Initiatives, The University of Osaka, Osaka, Japan. ✉e-mail: y.kato.med@osaka-u.ac.jp; muramatsu@ncnp.go.jp

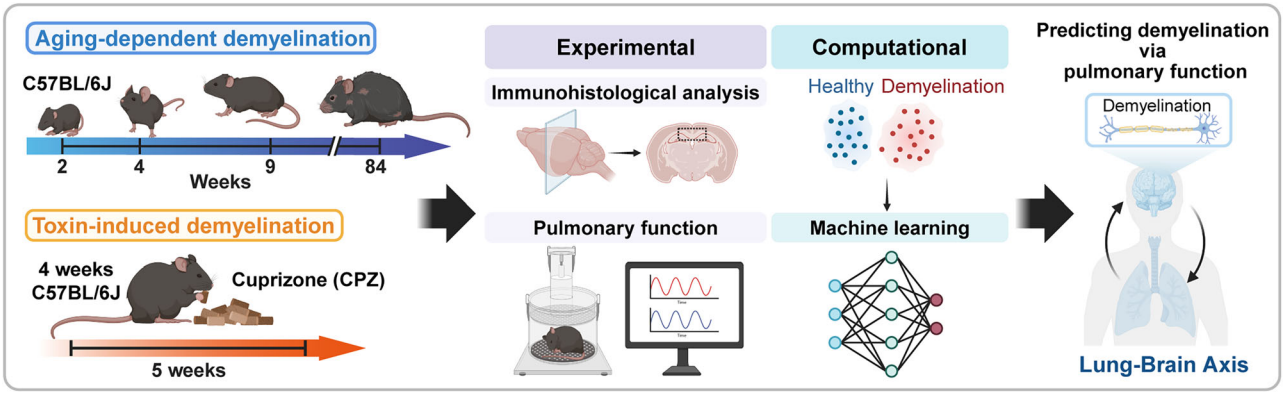

Fig. 1 | Experimental design. The study consists of two experimental paradigms to investigate the relationship between myelin morphology and respiratory function. In the developmental (aging) experiment, mice at different ages were evaluated for myelin content using immunostaining and respiratory function using whole-body plethysmography. In the pathological model, demyelination was induced by feeding mice a 0.2% cuprizone (CPZ)-containing diet for 5 weeks. Respiratory measurements and MBP staining were performed after treatment to assess disease-related changes. Data from each experiment were analyzed to determine correlations between respiratory parameters and myelin status. Some elements of this figure were created with BioRender.com (licensed to our institution).

on the gut–brain communication[15]. Obesity, a systemic condition characterized by altered inter-organ communication, may contribute to impaired cognitive function and an increased risk of dementia later in life[16]. Regarding myelin regulation, we previously reported that peripheral factors such as leptin[17] and fibroblast growth factor (FGF) 21[18], promote myelin repair following CNS injury. Among these factors, apelin—produced abundantly by the lungs—has been shown to promote myelin repair in both age-related and disease-associated demyelination[19]. Furthermore, accumulating evidence highlights various lung–brain interactions, including brain inflammation triggered by inhalation of lipopolysaccharide (LPS)[20], the association between aging of respiratory functions and cognitive decline[21], and even depression-like behaviors following lung resection in non-small-cell lung cancer[22]. These findings prompted us to hypothesize that myelin dynamics may be closely linked to the physiological state of peripheral organs such as the lungs, providing a novel perspective for understanding and detecting changes in CNS myelination.

In the present study, we aimed to explore whether morphological changes in myelin could be predicted based on respiratory function. We found that variations in myelin content within the corpus callosum could be predicted through integrative analysis of multiple respiratory parameters, including peak expiratory flow (PEFb), respiratory frequency (f), and pause (PAU), with these metrics emerging as key contributing factors. The integrative analysis could also be applied to predict demyelination in the brain of the mice fed cuprizone, a well-established demyelination reagent. These findings suggest that respiratory parameters may serve as a non-invasive and informative proxy for assessing myelin status in the brain.

Results

Association between age-dependent changes in myelination and respiratory parameters

To investigate the relationship between myelin morphology and respiratory parameters, we designed an experimental approach to visualize both developmental changes in myelin and pathological myelin loss, and to examine their association with respiratory function under each condition (Fig. 1). In this study, we used partially overlapping, but not identical, cohorts for respiratory measurements and MBP immunostaining. We first analyzed developmental changes in myelin content by performing immunohistochemical staining for myelin basic protein (MBP) in brain sections obtained from mice at different ages (2, 4, 9, and 84 weeks). Quantitative analysis revealed age-dependent changes in the MBP-positive area of the corpus callosum (Fig. 2A–C), consistent with previous findings showing that myelination increases from the early postnatal period up to adulthood, followed by a gradual decline in older mice[5]. Subsequently, respiratory function parameters of the mice (Table 1) were measured at the corresponding ages. Average values of each respiratory parameter were calculated over the observation period (Fig. 2D), and correlation analyses were performed between intergroup differences in these parameters and MBP levels (Table 2). Intergroup variations in parameters such as enhanced pause (Penh), pause (PAU), end inspiratory pause (EIP), time of pause (TP), and time of break (TB) showed a correlation with age-related changes in MBP (Penh, Spearman's $\rho = 0.8$, $p = 0.2$; PAU, Spearman's $\rho = 0.8$, $p = 0.2$; EIP, Spearman's $\rho = 1$, $p = 0$; TP, Spearman's $\rho = 0.8$, $p = 0.2$; and TB, Spearman's $\rho = -1$, $p = 0$). These findings suggest that respiratory function may be partly associated with myelin content in the brain.

Predicting myelin development by integrated respiratory parameter analysis

Since multiple respiratory parameters were associated with myelin content, we next explored the possibility of predicting myelin levels through an integrated analysis of these parameters. We used time-series measurements of respiratory parameters, treating each measured value obtained during the observation period as an individual data point, to examine whether respiratory function was associated with the state of myelination. To classify the mice into four age groups, three machine learning models, a kernel support vector machine (SVM), a k-nearest neighbor (KNN) classifier, and a random forest (RF), trained on the training dataset, were used. Permutation importance analysis for each classifier in the test set (Fig. 3A) identified PEFb and f as important features for group discrimination. The decision boundary of each machine learning model on the test set, retrained on data reduced to a 2-dimensional UMAP (uniform manifold approximation and projection) space (Fig. 3B), indicated reasonable predictive performance for each classifier. To quantitatively evaluate the performance of each classifier on the test set, we calculated the macro averages of precision, recall, and F1-score (Fig. 3C). These results indicate that integrative analysis of respiratory parameters may effectively predict age-related changes in myelin status across all three machine learning models.

Association of pathological demyelination with respiratory parameters

We next asked whether prediction by respiratory functions of myelin contents is not limited to the developmental change of myelin but also useful for the pathological change of myelin formation. Mice fed cuprizone-containing diets are widely used as demyelination models because they exhibit demyelination primarily in the corpus callosum, the largest myelinated region in the brain (Fig. 4A)[23]. In this study, we first confirmed demyelination in the corpus callosum of adult mice (9 weeks) fed cuprizone using MBP staining (Fig. 4B, C). We then measured spontaneous

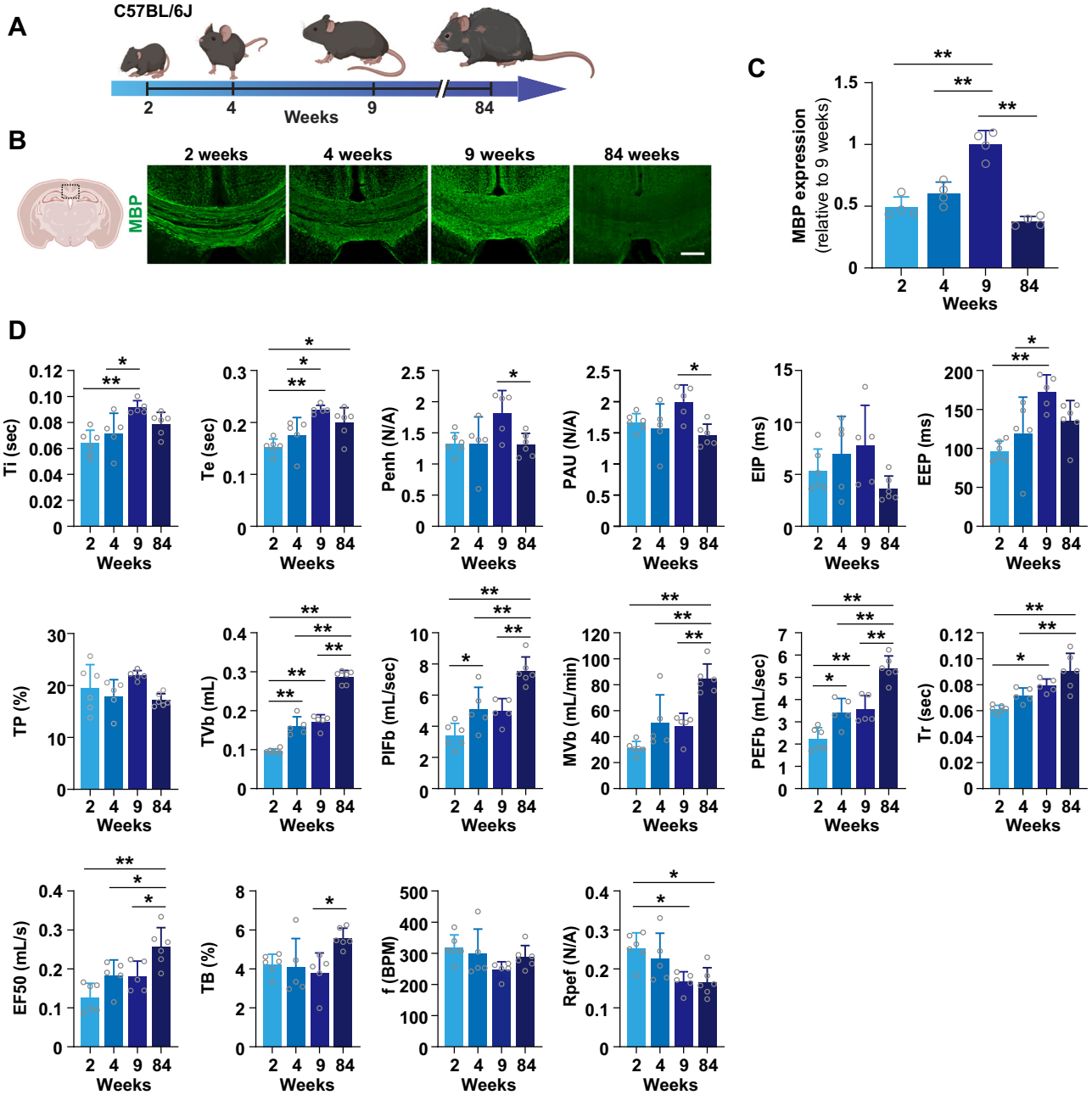

Fig. 2 | Changes in myelin formation and respiratory functions with aging. **A** Ages (weeks) of mice used in each experimental group. **B** Representative images of brain sections from the mice at indicated ages. Sections were labeled with MBP. **C** Quantification of MBP expression in the corpus callosum in the indicated age of mice ($n = 4$). **D** Quantification of respiratory function measures in the indicated age of mice ($n = 5$-6). Error bars represent mean ± SEM. Statistical analysis was performed using one-way ANOVA followed by Tukey's post-hoc test. $^{*}p < 0.05$, $^{**}p < 0.01$. n.s., not significant difference. The correlation between MBP expression and each respiratory parameter was analyzed using Spearman's rank correlation coefficient. Some elements of this figure were created with BioRender.com (licensed to our institution).

respiration in the same animals and recorded each respiratory parameter. Furthermore, we calculated the average values of each parameter and found no significant differences in any of the respiratory parameters between the cuprizone-treated and control groups (Fig. 4D). These findings suggest that average respiratory parameter values may be insufficient for predicting demyelination in disease-like conditions.

Predicting pathological demyelination by integrated respiratory parameter analysis

We assessed whether the respiratory measurements obtained during the observation period, treated as individual data points, were associated with the demyelination state. Three commonly used machine learning models (kernel SVM, KNN, and RF) were trained on the training dataset to perform binary classification (demyelination vs. control). Permutation importance analysis of each classifier on the test set (Fig. 5A) identified PAU as an important feature common to all three classifiers. The decision boundary of each machine learning model on the test set showed that all classifiers achieved good discrimination (Fig. 5B). The receiver operating characteristic (ROC) curves for the three classifiers showed that RF achieved the highest AUC (area under the ROC curve) (Fig. 5C). Collectively, these data demonstrate that integrative respiratory function analysis may provide a robust prediction of pathology-

Table 1 | Respiratory Function Measurements

Feature	Abbreviation	Unit	Definition	Machine learning
Inspiratory time	Ti	sec	Time from start to end of inspiration	
Expiratory time	Te	sec	Time from start to end of expiration	
Enhanced pause	*[1]Penh	N/A	Indicator of airway hyperresponsiveness	✓
Pause	*[2]PAU	N/A	Index of bronchoconstriction	✓
End inspiratory pause	EIP	ms	Pause between the end of inspiration and the start of expiration	✓
End expiratory pause	EEP	ms	Pause between the end of expiration and the start of next inspiration	✓
Time of pause	TP	%	Percentage of breath spent in the pause between expiration and inspiration	✓
Tidal volume	TV	mL	Inhaled volume per breath	
Peak inspiratory flow	PIFb	mL/sec	Maximum inspiratory flow rate during one breath	✓
Minute volume	*[3]MV	mL/min	Product of tidal volume (TV) and respiratory rate	
Peak expiratory flow	PEFb	mL/sec	Maximum expiratory flow rate during one breath	✓
Relaxation time	Tr	sec	Time from start of expiration until 70% of tidal volume is expired	
Expiratory flow at 50% of tidal volume	EF50	mL/sec	Expiratory flow rate at 50% of tidal volume; an indicator of bronchoconstriction	
Time of break	TB	%	Percentage of respiratory cycle spent in the pause between expiration and inspiration	
Respiratory frequency	f	breaths/min	Number of breaths per minute	✓
Ratio of time to peak expiratory Flow	*[4]Rpef	N/A	Ratio of time from start of exhalation to peak expiratory flow divided by expiratory time (Te)	✓

*[1]Penh = ((Te/Tr)-1) × PEFb/PIFb.
*[2]PAU = Te/Tr-1.
*[3]MV = TV × F.
*[4]Rpef = Time from the onset of expiration to PEF/Te.

Table 2 | Correlation coefficient between MBP expression and respiratory function

	Pearson correlation coefficient	Kendall's rank correlation coefficient	Spearman's rank correlation coefficient
Ti	0.673	0.333	0.4
Te	0.588	0.333	0.4
Penh	0.921	0.667	0.8
PAU	0.929	0.667	0.8
EIP	0.916	1	1
EEP	0.708	0.333	0.4
TP	0.868	0.667	0.8
TVb	−0.321	0	−0.2
PIFb	−0.340	−0.333	−0.4
MVb	−0.408	−0.333	−0.4
PEFb	−0.299	0	−0.2
Tr	−0.079	0	−0.2
EF50	−0.298	−0.333	−0.4
TB	−0.806	−1	−1
f	−0.775	−0.333	−0.4
Rpef	−0.267	0	0.2

associated myelin alterations, with predictive utility that transcends model-specific limitations.

Discussion

In this study, we demonstrated that the integration of respiratory parameters enables the prediction of brain myelin status in mice under both physiological aging and pathological demyelination conditions. This finding suggests that peripheral physiological outputs, such as respiratory function, are functionally linked to the structure of central white matter. Although spontaneous respiration is primarily controlled by brainstem circuits[24], it is also regulated by descending myelinated pathways such as the corticobulbar and corticopontine tracts that originate in the motor cortex[25]. These tracts pass through the internal capsule and cerebral peduncle, serving as conduits between the cortex and respiratory centers. Thus, changes in their myelination may alter signal transmission and manifest as changes in respiratory output. In the aging model, we found that the average values of specific respiratory parameters were correlated with myelin levels, and integrative analysis further identified "PEFb" and "f" as particularly effective predictors. These results suggest that combining multiple parameters can enhance classification accuracy. Interestingly, some respiratory parameters remained unchanged even in older mice with reduced myelin levels, indicating that age-related alterations in respiratory parameters are not uniform. As respiratory function is governed by multiple cell types that undergo both intracellular and extracellular age-related changes, it is plausible that the extent of age-associated variation differs by parameter depending on the balance of contributing factors. This interpretation is consistent with the previously reported phenomenon of cell–type–specific aging within the same organ[26].

To model demyelination with pathological conditions, we employed cuprizone-induced demyelination in mice. In this model, while average values of respiratory parameters did not differ significantly between control and demyelinated mice, specific parameters such as "PAU" contributed strongly to classification accuracy via machine learning. This suggests that pathological demyelination induces changes in respiratory control that are not reflected in mean values. The differences in respiratory profiles between the aging and disease models may reflect not only variations in factors associated with pathological features, such as inflammation, but also differences in the rate of demyelination. Gradual myelin loss during aging may allow time for functional adaptation, whereas abrupt pathological demyelination may lead to the capacity for neural compensation being exceeded, unmasking latent dysfunction. Although OPCs are preserved and maintain their proliferative capacity in aged animals[27], OPC loss has been reported in

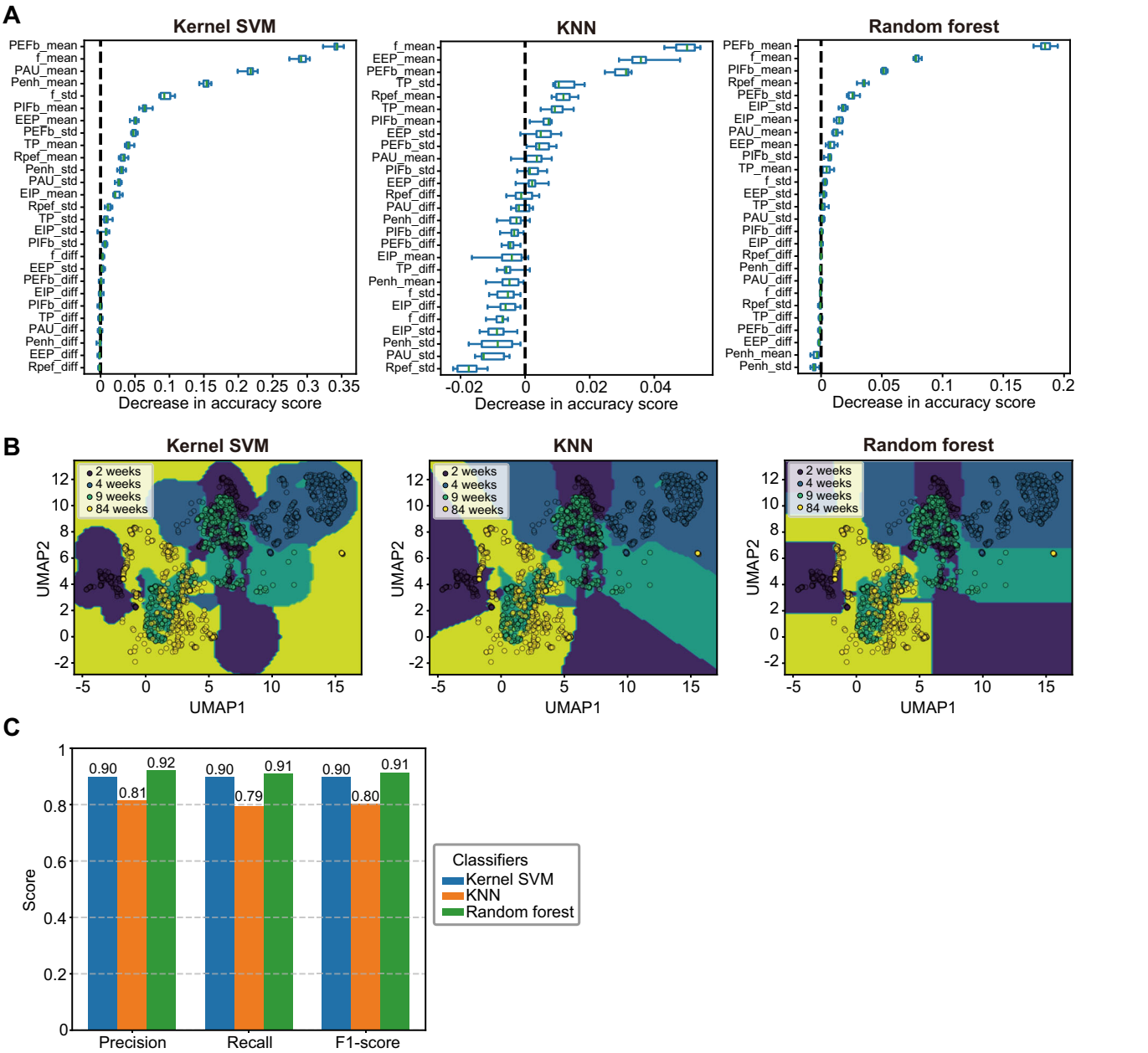

Fig. 3 | Predictive performance of the aging model using supervised machine learning. A Permutation importance on the test set for the three classifiers. **B** Decision boundaries on the test set for the three classifiers. **C** Performance comparison among the three classifiers based on macro averages of precision, recall, and F1-score.

disease models[28]. Moreover, oligodendrocytes contribute not only to myelination but also to BBB maintenance[29] and metabolic support for surrounding cells, including neurons[30], suggesting that CNS–lung communication may be affected by mechanisms beyond MBP level changes. Reports of the "clinico-radiological paradox", in which demyelination or axonal damage occurs without overt clinical symptoms[31], also support the idea that compensatory neural mechanisms are at play. Notably, the ability to predict myelin status from respiratory data in both aging and disease models highlights the robustness and generalizability of this phenomenon. Despite differences in the demyelination mechanisms and kinetics, the consistent classification accuracy across models suggests that respiratory patterns universally reflect white matter integrity in the brain.

This study has several limitations. First, our machine learning evaluation primarily reflects within-subject temporal prediction. Because the train-test split was performed chronologically within each animal, generalization to completely unseen subjects remain untested, and the models may capture subject-specific patterns that do not readily generalize. Second, respiratory measurements and MBP immunostaining were conducted in partially overlapping, but not identical, cohorts. Although animals were matched by age and treatment duration, the absence of fully paired datasets limits the ability to perform individual-level correlations between respiratory features and myelin status. Third, limitations inherent to the cuprizone model should be noted. Although demyelination is most prominent in the corpus callosum, other white matter regions are also affected, and cuprizone targets not only oligodendrocytes but also other glial and immune cells[32]. Thus, more selective approaches, such as toxin-induced focal demyelination or oligodendrocyte-specific depletion, would be required to draw conclusions that are strictly corpus callosum- or oligodendrocyte-specific. Fourth, MBP immunostaining reflects myelin protein abundance but does not provide detailed information on ultrastructural morphology. We did not incorporate numerical data derived from electron microscopy into the current machine learning models, which were constructed solely based on MBP-derived

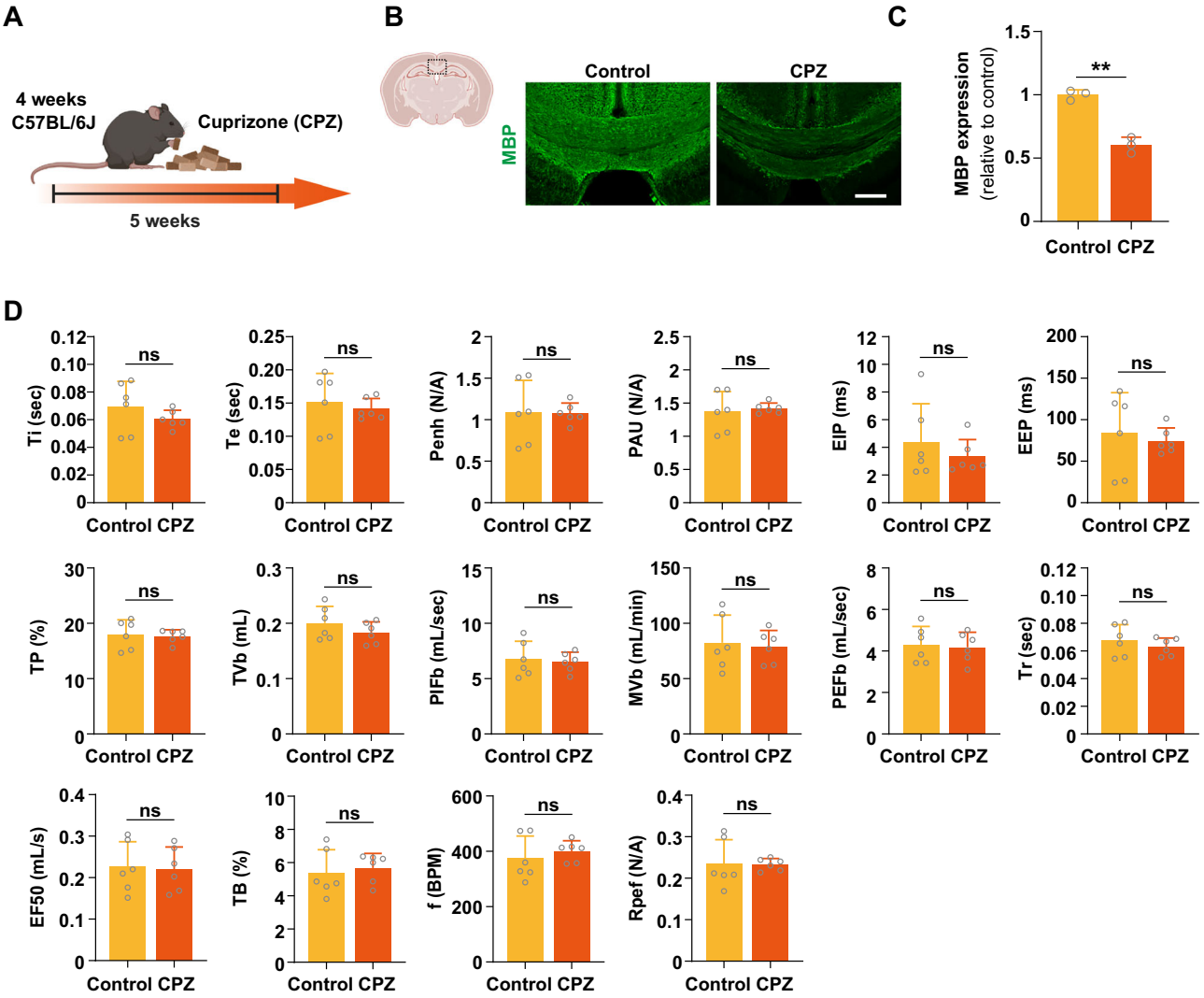

Fig. 4 | Changes in myelin formation and respiratory functions in CPZ-treated demyelination mice. A Condition of mice used in this experiment. **B** Representative images of brain sections from the mice with or without CPZ treatment. Sections were labeled with MBP. **C** Quantification of MBP expression in the corpus callosum of each mouse ($n = 3$). **D** Quantification of respiratory function measures of each mouse ($n = 6$). Error bars represent mean ± SEM. Statistical analysis was performed using Student's t-test. $^{**}p < 0.01$. n.s., not significant difference. Some elements of this figure were created with BioRender.com (licensed to our institution).

measures. Therefore, it remains unclear whether the same models could accurately predict other indices of myelin integrity. Finally, although the corpus callosum ROI was defined with reference to a standard atlas, we cannot completely exclude minor involvement of adjacent white matter in the MBP quantification, which should be considered when interpreting the results.

Despite these limitations, our findings provide new evidence supporting the concept of the "lung-brain axis," in which bidirectional communication between the respiratory and nervous systems plays a functional role. Notably, the lungs have been shown to regulate brain function via humoral factors. For instance, the lung microbiome modulates autoimmune inflammation in the brain in experimental autoimmune encephalomyelitis (EAE), an animal model of MS[33]. Apelin, a lung-derived secreted factor, promotes central myelin repair under both aging and pathological conditions[19]. In contrast, the present study revealed a functional association between respiratory dynamics and myelin status in the brain. This finding supports the concept that inter-organ communication is mediated not only by molecular signaling but also by systemic physiological outputs such as peripheral respiratory patterns. The fact that a physiological and non-invasive parameter like breathing pattern can be used to estimate CNS white matter status offers significant potential for future clinical applications. In the future, comparing respiratory data with MRI findings in elderly individuals or patients with demyelinating diseases such as MS may enable the development of simple, non-invasive screening and monitoring tools. Respiratory parameters may also serve to predict the efficacy of remyelination therapies, such as clemastine[34], and to guide therapeutic decisions. More broadly, this approach could lead to the development of generalizable biomarkers applicable to several CNS diseases, including dementia and depression, with the potential for early diagnosis, disease monitoring, and therapeutic evaluation.

Methods

Mice

All experimental procedures were approved by the Committee on the Ethics of Animal Experiments of the National Institute of Neuroscience, National Center of Neurology and Psychiatry (2024030R1). Male C57BL/6 J mice were obtained from Tokyo Laboratory Animal Science and Japan SLC. Mice were housed in an air-conditioned room at 23 ± 1°C with a 12 h light–dark cycle under specific pathogen-free conditions. They had free access to water and standard chow throughout the study period. All analyses were performed by investigators blinded to the experimental groups. The experimental unit was a single mouse.

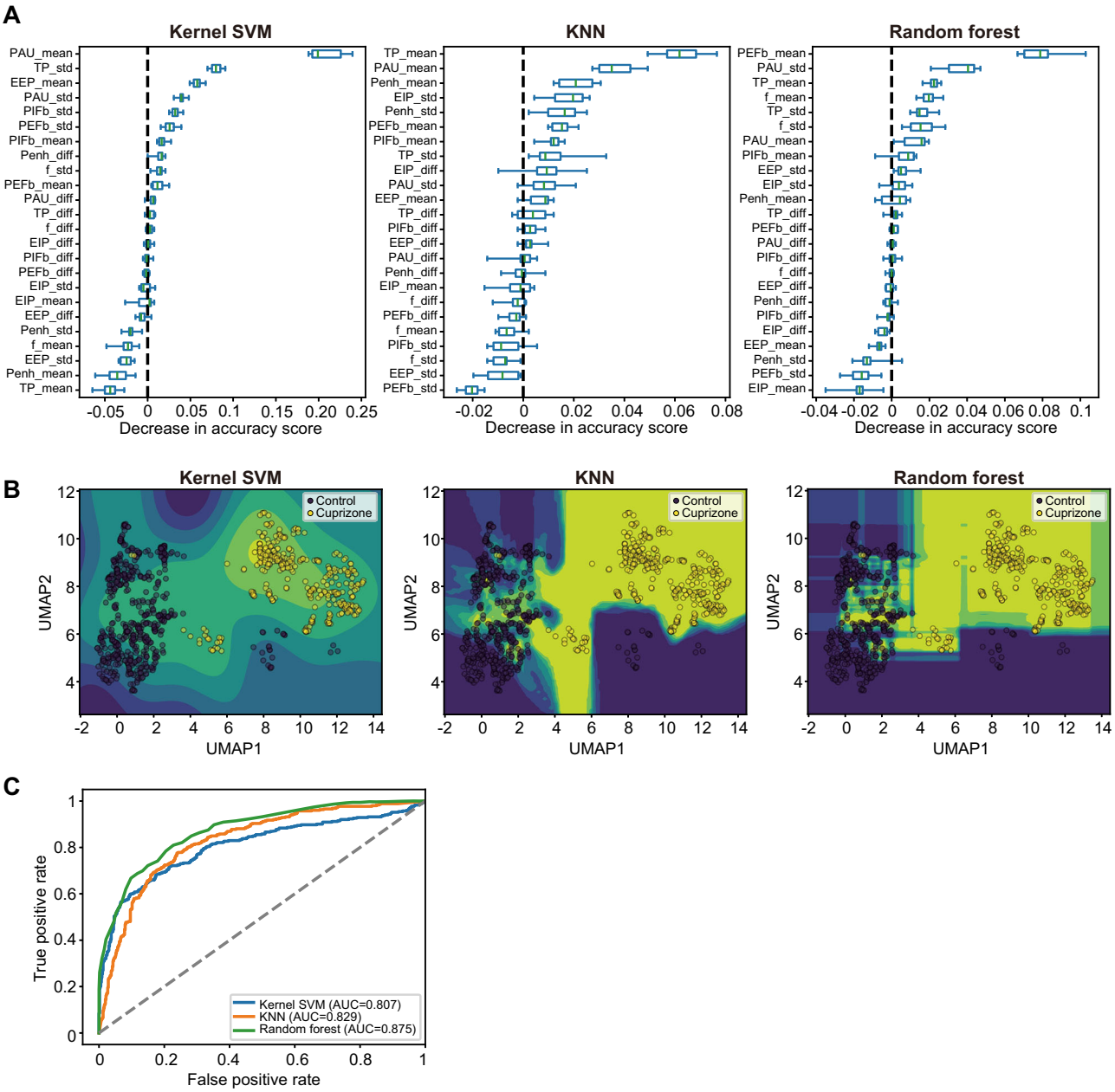

Fig. 5 | Predictive performance of the demyelination model using supervised machine learning. A Permutation importance on the test set for the three classifiers. **B** Decision boundaries on the test set for the three classifiers. **C** Receiver operating characteristic (ROC) curves for the three classifiers with corresponding AUC (area under the ROC curve) values.

Cuprizone-induced demyelination model

Four-week-old mice were fed a diet containing 0.2% (w/w) cuprizone (Sigma-Aldrich, C9012) for 5 weeks[35]. The cuprizone-containing diet was refrigerated and replaced with fresh food every day. Experimental units were randomly assigned to control and treatment groups by the experimenter. Throughout the experimental period, body weight was monitored, and the changes observed were consistent with those reported previously (data not shown)[36,37]. Body weight was not included as a covariate in the analyses.

Immunohistochemistry

Mice were transcardially perfused with phosphate-buffered saline (PBS), followed by 4% paraformaldehyde in PBS. The brains were subsequently immersed in 20% and then 30% sucrose in PBS, each for 24 hours at 4°C. The tissues were embedded in Tissue-Tek® O.C.T. Compound (Sakura Finetek), and serial coronal sections (25 µm thick) were cut in the anterior-to-posterior direction from bregma −0.13 mm to −2.3 mm and mounted on TOMO® Adhesion Microscope Slides (Matsunami Glass). For myelin basic protein (MBP) staining, sections were incubated in PBS containing 0.3% Triton X-100 and 3% normal donkey serum for 30 minutes at room temperature. The sections were incubated with anti-MBP antibody (1:400, Abcam, ab7349), followed by Alexa Fluor 488-conjugated donkey anti-rat IgG secondary antibody (1:500, Thermo Fisher Scientific, A21208) for 2.5 hour at room temperature. Images were acquired using a fluorescence microscopes (Olympus, BX53, FV3000).

To quantify the MBP-positive area, we used ImageJ (National Institutes of Health) to calculate the proportion of MBP-positive regions within the corpus callosum. MBP-positive regions were defined as pixels exceeding a predetermined signal threshold. The corpus callosum ROI was delineated with reference to a standard mouse brain atlas, ensuring that the entire corpus callosum was consistently included across animals.

For each animal, the mean MBP-positive area was obtained from at least six coronal sections, each spaced at least 100 µm apart. No explicit adjustment was made for age-related differences in overall brain size. Quantification was performed using sections of anatomically matched coronal levels for all animals. Each section was confirmed to have uniform staining quality across samples using Black Gold, an independent myelin marker (data not shown).

Whole-body plethysmography

Respiratory function was assessed using unrestrained whole-body plethysmography (2-Site System-Mouse, Buxco® FinePointe, DSI) in conscious, freely moving mice. Before measurement, mice were acclimated to the plethysmography chamber for 5 minutes, and respiratory parameters were recorded for 60 minutes under room air conditions. All measurements were performed during the light cycle at room temperature, and animals were monitored throughout the procedure to minimize stress. All parameters were automatically calculated, collected, and analyzed using the associated FinePointe Software (DSI). Each parameter was averaged over a 10-second interval, and the mean value from each interval was treated as a single data point.

Preprocessing of respiratory data

For the respiratory data obtained from both aging and demyelination models, a rejection index (Rinx) was employed to filter out unreliable data points within continuous time intervals. The Rinx is defined as the ratio of excluded wave counts to total wave counts within a 10-second interval. Specifically, the longest interval with a median Rinx ≤ 20% was selected backward from the final data point, as data collected during later time intervals tend to be more reliable than those from earlier intervals. Subsequently, among the 20 parameters (features) obtained from the system, environmental parameters and derived features calculated from other features were excluded. Features with variance < 0.001 across all samples were also removed. For the time-series analysis, only trending data points were selected by calculating autocorrelation for each feature, yielding a maximum of nine features (Table 1). Missing values and outliers were then addressed through linear interpolation. Finally, a sliding window of size 10 was applied across the entire time interval with a step size of one to compute the mean and standard deviation of each feature. Additionally, the difference between adjacent data points was incorporated as a new feature. To ensure comparability across features, each feature was standardized. The total number of data points was 6873 for the aging model and 3043 for the demyelination model.

Supervised machine learning

Each preprocessed dataset from the two models was split into training and test sets at a ratio of 70% to 30%, respectively. The training set was temporally positioned before the test set, and stratification was performed to preserve class label proportions. The main reason for this setting is that our primary objective is to predict future states/labels from preceding temporal patterns within the same subject, which reflects the intended real-world application of our model. In clinical or monitoring scenarios, the model would be deployed to forecast future outcomes for an individual based on their own historical data. Therefore, our evaluation focuses on temporal generalization (predicting unseen time points) rather than cross-subject generalization (predicting unseen individuals). On the other hand, there are a few limitations: (1) our current evaluation does not fully address the model's performance on completely unseen animals/subjects. The reported metrics primarily reflect within-subject temporal prediction capability, and (2) the model may capture subject-specific patterns that do not generalize to new individuals.

We then employed three supervised machine learning models: a kernel support vector machine (SVM) with a radial basis function, a k-nearest neighbor (KNN) classifier, and a random forest (RF) algorithm. The hyperparameters for each machine learning model were optimized using grid search with 5-fold cross-validation that accounted for the time-series nature of the data. To evaluate predictive performance, we used precision and recall metrics. Precision is calculated as the ratio of true positives to all positive predictions, and recall is calculated as the ratio of true positives to all actual positives. In addition, to assess balanced performance, we used the F1-score, which is defined as the harmonic mean of precision and recall metrics.

Statistical analysis

All statistical analyses are detailed in the figure legends. Student's *t*-test and one-way analysis of variance (ANOVA) followed by Tukey–Kramer post hoc test were performed using Prism 10 (GraphPad software). A p-value < 0.05 was considered statistically significant. Data are presented as mean ± standard errors of the mean.

Language editing

ChatGPT (OpenAI) was used for language editing. The authors are fully responsible for the final content.

Data availability

All the data analyzed and presented in this study are available from the authors upon reasonable request.

Received: 25 August 2025; Accepted: 10 December 2025;
Published online: 02 February 2026

References

1. Osso, L. A. & Hughes, E. G. Dynamics of mature myelin. *Nat. Neurosci.* **27**, 1449–1461 (2024).
2. Jakimovski, D. et al. Multiple sclerosis. *Lancet* **403**, 183–202 (2024).
3. Nasrabady, S. E., Rizvi, B., Goldman, J. E. & Brickman, A. M. White matter changes in Alzheimer's disease: a focus on myelin and oligodendrocytes. *Acta Neuropathol. Commun.* **6**, 22 (2018).
4. Depp, C. et al. Myelin dysfunction drives amyloid-β deposition in models of Alzheimer's disease. *Nature* **618**, 349–357 (2023).
5. de Faria, O. et al. Periods of synchronized myelin changes shape brain function and plasticity. *Nat. Neurosci.* **24**, 1508–1521 (2021).
6. Ramos-Cabrer, P. et al. Reversible reduction in brain myelin content upon marathon running. *Nat. Metab.* **7**, 697–703 (2025).
7. Tamura, M. K. & Yaffe, K. Dementia and cognitive impairment in ESRD: diagnostic and therapeutic strategies. *Kidney Int* **79**, 14–22 (2011).
8. Mueller, K. et al. Brain Damage With Heart Failure Cardiac Biomarker Alterations and Gray Matter Decline. *Circ. Res* **126**, 750–764 (2020).
9. Bouhrara, M. et al. Evidence of association between obesity and lower cerebral myelin content in cognitively unimpaired adults. *Int J. Obes.* **45**, 850–859 (2021).
10. Franklin, R. J. M. & Ffrench-Constant, C. Remyelination in the CNS: From biology to therapy. *Nat. Rev. Neurosci.* **9**, 839–855 (2008).
11. Van Der Weijden, C. W. J. et al. Quantitative myelin imaging with MRI and PET: an overview of techniques and their validation status. *Brain* **146**, 1243–1266 (2023).
12. Philips, T. & Rothstein, J. D. Oligodendroglia: metabolic supporters of neurons. *J. Clin. Invest* **127**, 3271–3280 (2017).
13. Fischer, R., Wajant, H., Kontermann, R., Pfizenmaier, K. & Maier, O. Astrocyte-specific activation of TNFR2 promotes oligodendrocyte maturation by secretion of leukemia inhibitory factor. *Glia* **62**, 272–283 (2014).
14. Xiao, J. et al. Brain-derived neurotrophic factor promotes central nervous system myelination via a direct effect upon Oligodendrocytes. *Neurosignals* **18**, 186–202 (2011).
15. Cryan, J. F. et al. The microbiota-gut-brain axis. *Physiol. Rev.* **99**, 1877–2013 (2019).
16. Dye, L., Boyle, N. B., Champ, C. & Lawton, C. The relationship between obesity and cognitive health and decline. *Proc. Nutr. Soc.* **76**, 443–454 (2017).
17. Matoba, K., Muramatsu, R. & Yamashita, T. Leptin sustains spontaneous remyelination in the adult central nervous system. *Sci. Rep.* **7**, 1–11 (2017).

18. Kuroda, M. et al. Peripherally derived FGF21 promotes remyelination in the central nervous system. *J. Clin. Invest* **127**, 3496–3509 (2017).
19. Ito, M. et al. Age-dependent decline in remyelination capacity is mediated by apelin–APJ signaling. *Nat. Aging* **1**, 284–294 (2021).
20. Kang, H. et al. Pulmonary flora-derived Lipopolysaccharide mediates lung-brain axis through activating microglia involved in polystyrene microplastic-induced cognitive dysfunction. *Adv. Sci.* **11**, 2404966 (2024).
21. Grande, G. et al. Lung function in relation to brain aging and cognitive transitions in older adults: A population-based cohort study. *Alzheimer's. Dement.* **20**, 5662–5673 (2024).
22. Uchitomi, Y. et al. Depression and psychological distress in patients during the year after curative resection of non-small-cell lung cancer. *J. Clin. Oncol.* **21**, 69–77 (2003).
23. Zirngibl, M., Assinck, P., Sizov, A., Caprariello, A. V. & Plemel, J. R. Oligodendrocyte death and myelin loss in the cuprizone model: an updated overview of the intrinsic and extrinsic causes of cuprizone demyelination. *Mol. Neurodegener.* **17**, 1–28 (2022).
24. Smith, J. C., Ellenberger, H. H., Ballanyi, K., Richter, D. W. & Feldman, J. L. Pre-Bötzinger Complex: a Brainstem Region that May Generate Respiratory Rhythm in Mammals. *Science* **254**, 726–729 (1991).
25. Krohn, F. et al. The integrated brain network that controls respiration. *Elife* **12**, e83654 (2023).
26. Koenig, A. L. et al. Single-cell transcriptomics reveals cell-type-specific diversification in human heart failure. *Nat. Cardiovasc. Res.* **1**, 263–280 (2022).
27. Ruckh, J. M. et al. Rejuvenation of regeneration in the aging central nervous system. *Cell Stem Cell* **10**, 96–103 (2012).
28. Kirby, L. et al. Oligodendrocyte precursor cells present antigen and are cytotoxic targets in inflammatory demyelination. *Nat. Commun.* **10**, 1–20 (2019).
29. Niu, J. et al. Aberrant oligodendroglial–vascular interactions disrupt the blood–brain barrier, triggering CNS inflammation. *Nat. Neurosci.* **22**, 709–718 (2019).
30. Fünfschilling, U. et al. Glycolytic oligodendrocytes maintain myelin and long-term axonal integrity. *Nature* **485**, 517–521 (2012).
31. Barkhof, F. The clinico-radiological paradox in multiple sclerosis revisited. *Curr. Opin. Neurol.* **15**, 239–245 (2002).
32. Zirngibl, M. et al. Oligodendrocyte death and myelin loss in the cuprizone model: an updated overview of the intrinsic and extrinsic causes of cuprizone demyelination. *Mol. Neurodegener.* **17**, 34 (2022).
33. Hosang, L. et al. The lung microbiome regulates brain autoimmunity. *Nature* **603**, 138–144 (2022).
34. Green, A. J. et al. Clemastine fumarate as a remyelinating therapy for multiple sclerosis (ReBUILD): a randomised, controlled, double-blind, crossover trial. *Lancet* **390**, 2481–2489 (2017).
35. Uyeda, A. et al. Dimethylarginine dimethylaminohydrolase 1 as a novel regulator of oligodendrocyte differentiation in the central nervous system remyelination. *Glia* **69**, 2591–2604 (2021).
36. Zhen, W. et al. An alternative cuprizone-induced demyelination and remyelination mouse model. *ASN Neuro* **9**, 759091417725174 (2017).
37. Toomey, L. M. et al. Cuprizone feed formulation influences the extent of demyelinating disease pathology. *Sci. Rep.* **11**, 22594 (2021).

Acknowledgements

We appreciate Prof. Yukio Kawahara and Yuki Inagaki to support the study. This study was supported by grants from the AMED-CREST (JP23gm1510009) to R.M. and S.S.; AMED-PRIME (JP21gm6510006) to S.S.; Intramural Research Grant (5-4) for Neurological and Psychiatric Disorders of NCNP to R.M. and Y.K.; Grant-in-Aid of Scientific Research (B) from the Japan Society for the Promotion of Sciences (JP24K03032) to Y.K.; Grant-in-Aid of Scientific Research (C) from the Japan Society for the Promotion of Sciences (JP21K12109) to Y.K.; Grant-in-Aid for Research Activity Start-up from the Japan Society for the Promotion of Sciences (JP24K23304) to K.N. Schematic representations were generated with Biorender (https://biorender.com/).

Author contributions

K.N. contributed the analysis. K.Hitomi and R.S. performed the analysis. K.Higuchi, A.U., K.O., M.N., and S.S. conducted the experiments. L.Q. supported preparing figures. Y.K. and R.M. wrote the manuscript and directed the project. All authors approved the manuscript.

Competing interests

The authors declare no competing interests.

Additional information

Correspondence and requests for materials should be addressed to Yuki Kato or Rieko Muramatsu.

Reprints and permissions information is available at http://www.nature.com/reprints

Publisher's note Springer Nature remains neutral with regard to jurisdictional claims in published maps and institutional affiliations.

Open Access This article is licensed under a Creative Commons Attribution-NonCommercial-NoDerivatives 4.0 International License, which permits any non-commercial use, sharing, distribution and reproduction in any medium or format, as long as you give appropriate credit to the original author(s) and the source, provide a link to the Creative Commons licence, and indicate if you modified the licensed material. You do not have permission under this licence to share adapted material derived from this article or parts of it. The images or other third party material in this article are included in the article's Creative Commons licence, unless indicated otherwise in a credit line to the material. If material is not included in the article's Creative Commons licence and your intended use is not permitted by statutory regulation or exceeds the permitted use, you will need to obtain permission directly from the copyright holder. To view a copy of this licence, visit http://creativecommons.org/licenses/by-nc-nd/4.0/.

© The Author(s) 2025